Structural Modulation and Direct Measurement of Subnanometric Bimetallic PtSn Clusters Confined in Zeolites

Lichen Liu,[1] Miguel Lopez-Haro,[2] Christian W. Lopes,[1] Sergio Rojas-Buzo,[1] Patricia Concepcion,[1] Ramón Manzorro,[2] Laura Simonelli,[3] Aaron Sattler,[4] Pedro Serna,[4] Jose J. Calvino[2] and Avelino Corma[1]*

[1] *Instituto de Tecnología Química, Universitat Politècnica de València-Consejo Superior de Investigaciones Científicas, Av. de los Naranjos s/n, Valencia 46022, Spain*

[2] *Departamento de Ciencia de los Materiales e Ingeniería Metalúrgica y Química Inorgánica, Facultad de Ciencias, Universidad de Cádiz, Cádiz, Spain*

[3] *ALBA Synchrotron Light Source, 08290 Cerdanyola del Vallès, Barcelona, Spain*

[4] *ExxonMobil Research and Engineering, Annandale, New Jersey, 08801, USA*

*Corresponding author. Email: acorma@itq.upv.es

Abstract

Modulating the structures of subnanometric metal clusters at the atomic level is a great synthetic and characterization challenge in catalysis. Here we show how the catalytic properties of subnanometric Pt clusters (0.5-0.6 nm) confined in the sinusoidal 10R channels of purely siliceous MFI zeolite modulate upon introduction of partially reduced Sn species that interact with the noble metal at the metal/support interface. The low mobility of Sn in H_2 over an extended period of time (>6 h) even at high temperatures (e.g. 600 ºC), which is determined by only a few additional Sn atoms added to the Pt clusters. Such structural features, which are not immediately visible by conventional characterization techniques and can be laid out after combination of in situ EXAFS, HAADF-STEM and CO-IR data, is key to provide one-order of magnitude lower deactivation rate in the propane dehydrogenation reaction while maintaining high intrinsic (initial) catalytic activity.

Introduction

It has been demonstrated in numerous systems that the introduction of a second metal into nanoparticulated metal catalysts can significantly modulate the electronic structure of pristine metals and further influence their catalytic behavior[1]. Furthermore, the electronic structures and surface properties of the bimetallic nanoparticles are strongly dependent on the spatial distribution of the two elements. By tuning the way of preparing the bimetallic nanoparticles or by post-synthesis treatments, the spatial distribution of the two elements as well as their chemical states can be modified and, thus, their reactivity[2-4]. Under reaction conditions, structural transformation and reconstruction of the metal ensembles may also occur, which can result in further changes of the catalytic behavior with time on stream.

Pt-based materials are widely used for reforming, hydrogenation and dehydrogenation catalysis in numerous industrial processes, due to their excellent properties for the activation of C-H bonds, while limiting the extend of C-C bond cleavage via hydrogenolysis[5]. Nonetheless, a second metal is typically incorporated together with Pt to further improve the selectivity and/or stability, particularly when the reaction temperature needs to be high (e.g. endothermic reactions). For instance, Sn is introduced as a second metal for propane dehydrogenation to propylene in the UOP Oleflex™ process[6,7]. Pt and the second metal (in this work, Sn) can be found in bimetallic catalysts in the form of multiple structures that range from completely segregated phases of each metal to perfectly mixed (Pt/Sn) alloys[8]. Optimal catalyst preparation is achieved when the C-C bond cleavage is shut down with no or minimal loss of actives sites responsible for the reaction of interest (e.g. dehydrogenation). While PtSn alloys significantly promote the selectivity to propylene in propane dehydrogenation, it also reduces and/or modulates the active Pt sites, decreasing the catalytic activity[5].

The structure of bimetallic PtM catalysts (M=Ga, Zn, In or Sn) has been studied by *in situ* XRD and *in situ* XAS. High Sn content and high activation temperature favor the formation of alloyed structures that significantly promote catalyst selectivity and stability in dehydrogenation reactions[8]. However, the resulting large alloyed PtM particles are suboptimal from an activity standpoint, and there is an interest to design more active, selective and stable subnanometric bimetallic catalysts[9-12]. In this respect, taking advantage of the confinement effect of zeolite structures, subnanometric metal species (single atoms and clusters with a few atoms) can be generated and stabilized in the porous

structures within the zeolite crystallites[13-17].

In this work, we investigate how modulating the exact interaction between the Pt and Sn in these subnanometric PtSn clusters (0.5-0.6 nm), located regioselectively at the sinusoidal 10R channel of the pure silica MFI zeolite, is key to achieve optimal catalytic performance. To understand the interaction between the subnanometric Pt and Sn species, we have applied several characterization techniques, including XAS, *quasi in situ* transmission electron microscopy and CO-IR spectroscopy. It will be shown, subtle changes in the structural features of the subnanometric PtSn clusters, which are not immediately visible by conventional spectroscopic techniques, can drastically affect their performance for propane dehydrogenation.

Results

Characterization of PtSn clusters in MFI zeolite

Initially, a K-PtSn@MFI-Air sample (containing 0.4 wt% of Pt, 0.9 wt% of Sn and 0.6 wt% of K) was prepared by a one-pot synthesis according to our reported synthesis method and then calcined in air, giving rise to the formation of atomically dispersed Pt and Sn species in pure-silica MFI zeolite[17]. As shown in **Figure 1a-1d** and **Supplementary Figures 1 and 2**, the location of singly dispersed Pt atoms in the pristine K-PtSn@MFI-Air sample was determined by combination of high-resolution high-angle annular dark-field scanning transmission electron microscopy (HR HAADF-STEM) imaging and integrated differential phase contrast (iDPC) imaging, which can simultaneously obtain the location information of heavy elements (Pt in this work) by HAADF-STEM, and the structure of the zeolite by iDPC imaging under low-dose conditions[18,19]. To ensure the presence of atomically dispersed Pt atoms in the K-PtSn@MFI-Air sample, a reference K-MFI sample (without Sn or Pt) was measured and compared. As shown in Supplementary **Figure 3**, and considering the image simulation results shown in our previous work, the bright dots appearing in the HRSTEM images can be ascribed to Pt atoms[17].

The chemical states of Pt in the pristine K-PtSn@MFI-Air sample during the H_2 reduction treatment were investigated by *in situ* X-ray absorption spectroscopy. It was found that, regardless of the reduction time at 600 ºC, the Pt species in the K-PtSn@MFI-Air sample are completely reduced to metallic Pt at 600 ºC[14], as inferred by the intensity of the white line in the X-ray absorption near

edge structure (XANES) spectra compared with a Pt foil reference (**Figure 2a**), and the appearance of Pt-Pt contributions in the Extended X-ray Absorption Fine Structure (EXAFS) spectra (**Figure 2b** and **Table 1**). STEM images show that the majority of the metal reassembles as subnanometric clusters of 0.5-0.6 nm during the H_2 treatment. The size of Pt clusters remains virtually unaltered regardless of the reduction time from 0 to 22 h, indicating high structural robustness (**Supplementary Figures 4-9**). The average size of Pt species in K-PtSn@MFI after reduction at 600 ºC for 0-22 h was also analyzed by EXAFS (see fitting details on the Pt-edge EXAFS results in **Supplementary Figure S10**). As shown in **Table 1**, the coordination number of Pt-Pt remains unchanged around 6-7 for all reduction times. We note that a small fraction of larger particles co-exist with the very small clusters in all these samples, leading to an average EXAFS coordination number slightly larger than that one would expect for Pt clusters of 0.5-0.6 nm. However, the vast majority of Pt ensembles observed by electron microscopy are below 0.6 nm and remain stable regardless of the reduction time at 600 ºC. Analysis of the STEM-iDPC images indicates that the Pt clusters in these reduced K-PtSn@MFI samples are at the 10R sinusoidal channels, regardless of the time of H_2 reduction treatment at 600 ºC (**Figure 1e-1t** and **Supplementary Figures 11-16)**

The nature of Sn species and their coordination environment in the K-PtSn@MFI samples was also studied by Sn-edge X-ray Absorption Spectroscopy. Sn is inferred to be Sn(IV) in the pristine K-PtSn@MFI-air sample, as indicated by the pronounced white line in the XANES spectra (**Figure 2c)**. Analysis of the EXAFS region (**Figure 2d**, **Table 1** and **Supplementary Figure 17**) shows the virtual lack of heavy backscatters in this sample (e.g. absence of Sn-O-Sn ensembles, which are otherwise observed in the bulk SnO_2 standard), which indicates that Sn is atomically dispersed inside the MFI. Additional ^{31}P MAS NMR data of adsorbed trimethylphosphine oxide (TMPO) on Pt-free K-Sn-MFI (prepared by the same procedure as the K-PtSn@MFI sample but without the addition of Pt precursor), show resonances at below 50 ppm (**Supplementary Figure 18)** that indicate that the vast majority of the Sn species is present as extra-framework species in the unreduced catalyst[20].

After treatment with H_2 from room temperature to 600 ºC, the Sn(IV) species reduces to Sn species with approximately three Sn-O bonds on average according to EXAFS (**Table 1**), and a white line intensity that matches that of Sn(II) in a bulk SnO standard. We infer that labile oxygen in the unreduced K-PtSn@MFI-Air sample reacted with H_2 to form Sn(II) species covalently bonded to oxygens from the support. The ^{31}P NMR spectrum of adsorbed TMPO confirms this observation, as

new bands at 50-60 ppm grow in H_2 that can be attributed to coordinately unsaturated SnO_{2-x}, which adsorb TMPO and give ^{31}P NMR signal in the same region as framework-type Sn species (**Supplementary Figure 18**)[20]. Within the sensitivity of XANES, the chemical states of Sn remain unchanged when the reduction time at 600 ºC is extended from 0 h to 22 h. Fitting of the EXAFS spectra also give almost the same Sn-O coordination number regardless of the reduction time (**Table 1** and **Supplementary Figure 17**). However, and interestingly, we observed drastic changes in the catalytic performance for propane dehydrogenation as a function of the reduction time (*vide infra*), which denote the occurrence of some structural changes when prolonging the exposure to H_2. The fraction of Sn responsible for the tuning the Pt catalytic properties appears to be too small to manifest using an average technique like EXAFS, where Sn-O contributions clearly dominate (see **Supplementary Discussion**).

In summary, neither the Pt L_{III}-edge nor the Sn K-edge EXAFS show evidence of any kind of bimetallic interactions in this series of samples, which show in contrast evident in literature reference samples when the two metals are well-alloyed[21-23]. Nevertheless, the presence of Sn in these catalysts has a strong effect on the catalytic properties of Pt, which will be discussed later in this work. Interestingly, these properties can be controlled by varying the reduction time, following a change in structure that is too subtle to be detected by EXAFS[24].

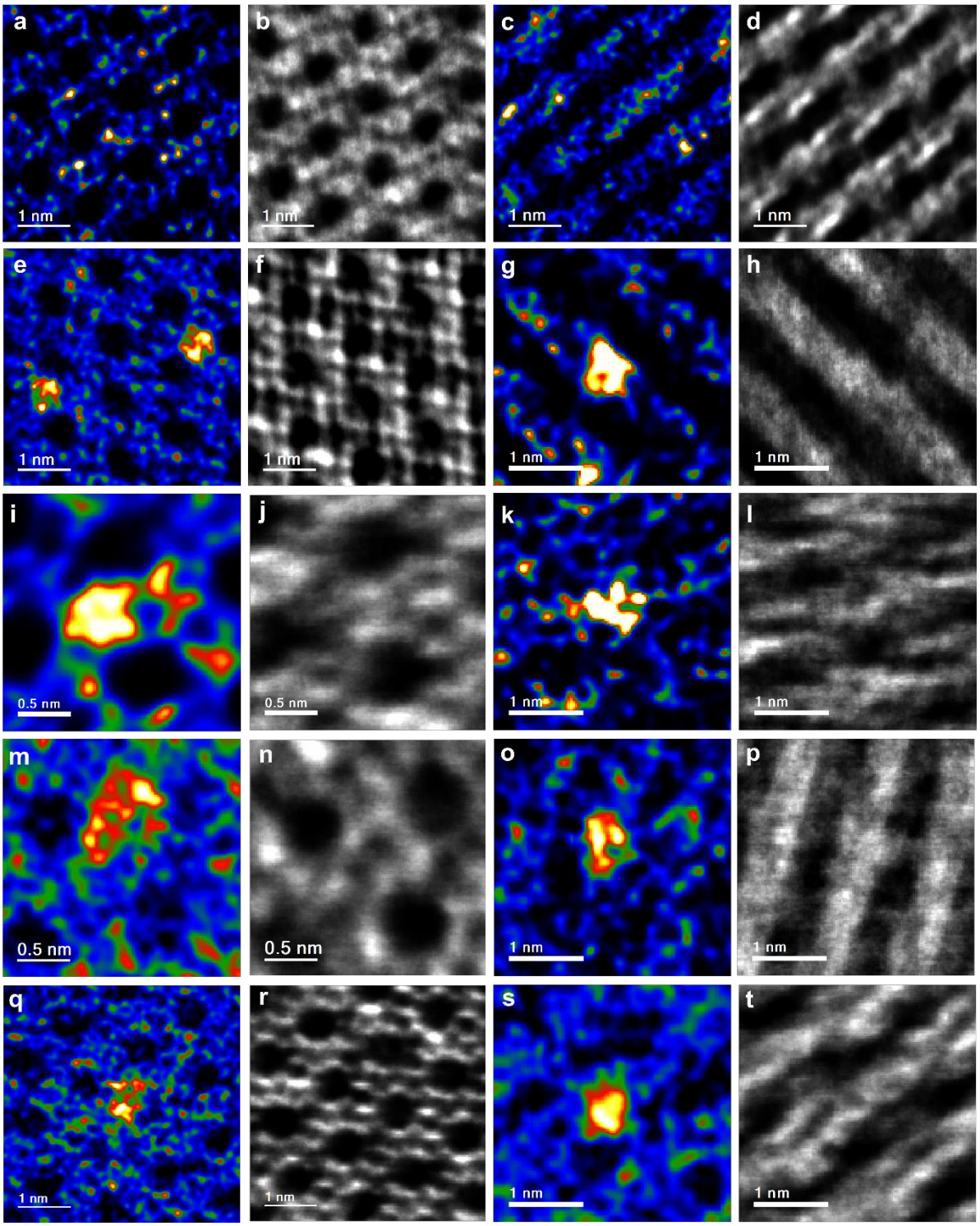

Figure 1. Identification of the location of subnanometric Pt species within the MFI structure. (a, c) high-resolution HAADF-STEM images and (b, d) the corresponding iDPC image of the same area of K-Pt@MFI-Air sample, showing the presence of singly dispersed Pt and Sn atoms in the sinusoidal channels. After reduction treatment by H_2 at 600 ^oC with increasing time, singly dispersed Pt and Sn atoms will agglomerate into subnanometric metal clusters in the 10R sinusoidal channels. (e-h) K-PtSn@MFI-600H_2-0h sample, (i-l) K-PtSn@MFI-600H_2-6h sample, (m-p)

K-PtSn@MFI-600H_2-12h sample, (q-t) K-PtSn@MFI-600H_2-22h sample.

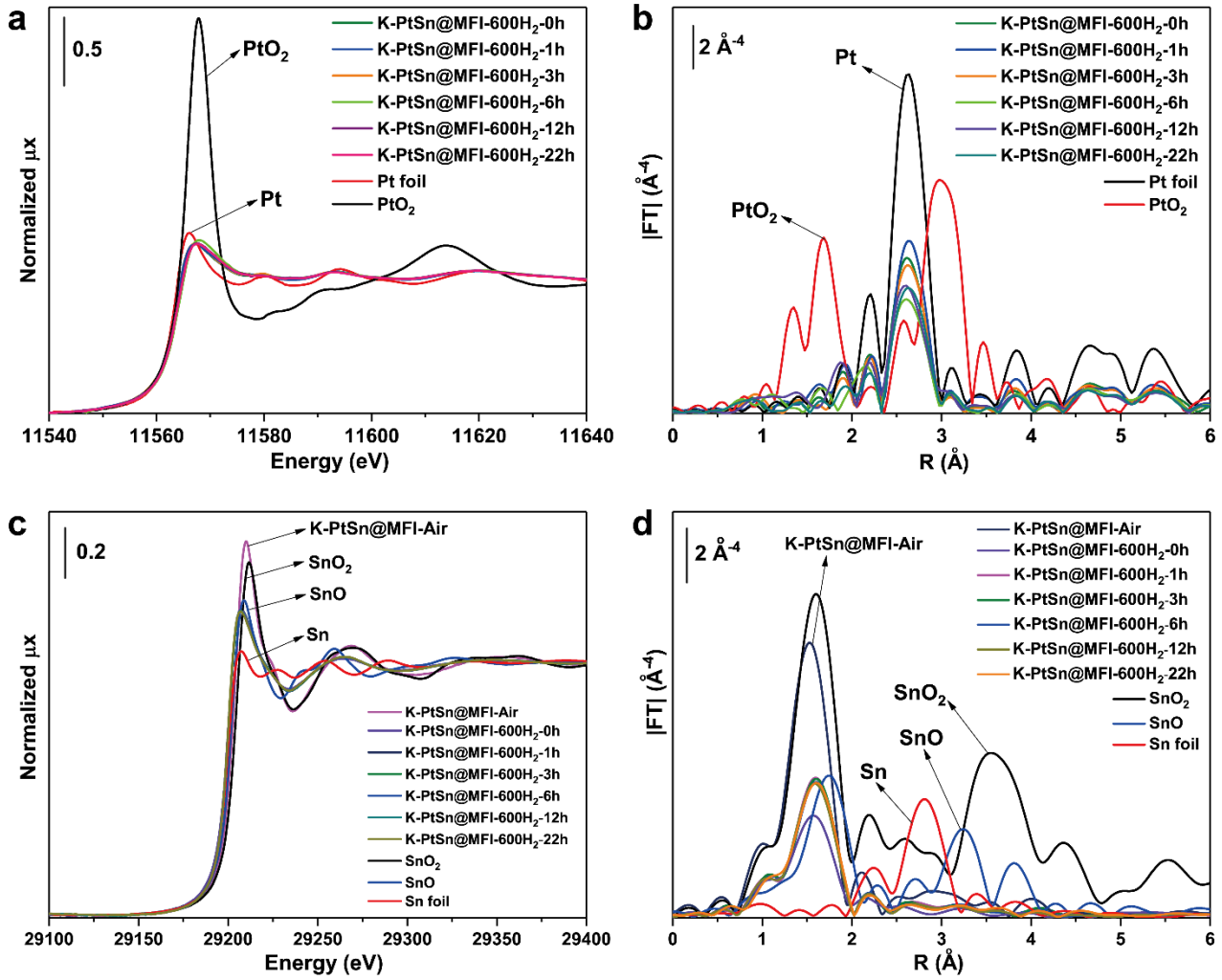

Figure 2. Characterizations of the chemical states and coordination environment of Pt and Sn. (a) Pt-edge XANES and (b) Pt-edge EXAFS spectra of the K-PtSn@MFI-600H_2 samples after different time of pre-reduction at 600 °C by H_2. (c) Sn-edge XANES spectra and (d) Sn-edge EXAFS spectra of the K-PtSn@MFI samples after different time of pre-reduction at 600 °C by H_2. The references are also included.

Table 1. Fit results of the Pt L_{III}-edge and Sn K-edge EXAFS data of various reduced K-PtSn@MFI catalysts.

Sample	N_{Pt-Pt}	R_{Pt-Pt} (Å)	σ^2 (Å^2)	ΔE_0 (eV)	R_{factor}
Pt foil[a]	12	2.763 ± 0.001	0.0048 ± 0.0001	6.7 ± 0.5	0.0017
K-PtSn@MFI-600H$_2$-0h[a]	6.6 ± 0.7	2.764 ± 0.003	0.0053 ± 0.0003	6.4 ± 0.8	0.0074
K-PtSn@MFI-600H$_2$-1h[a]	6.5 ± 0.6	2.767 ± 0.003	0.0050 ± 0.0003		0.0151
K-PtSn@MFI-600H$_2$-3h[a]	6.5 ± 0.6	2.767 ± 0.003	0.0054 ± 0.0003		0.0069
K-PtSn@MFI-600H$_2$-6h[a]	6.6 ± 0.9	2.761 ± 0.004	0.0063 ± 0.0006		0.0234
K-PtSn@MFI-600H$_2$-12h[a]	5.8 ± 0.6	2.766 ± 0.003	0.0055 ± 0.0004		0.0233
K-PtSn@MFI-600H$_2$-22h[a]	6.5 ± 0.6	2.764 ± 0.003	0.0059 ± 0.0005		0.0114

Sample	N_{Sn-O}	R_{Sn-O} (Å)	σ^2 (Å^2)	ΔE_0 (eV)	R_{factor}
SnO$_2$[b]	6	2.055 ± 0.010	0.0023 ± 0.0012	7.3 ± 1.4	0.0044
SnO[b]	4	2.202 ± 0.001	0.0071 ± 0.0012	8.3 ± 0.7	0.0017
K-PtSn@MFI-Air[b]	6.2 ± 0.2	2.022 ± 0.004	0.0038 ± 0.0005	4.5 ± 0.5	0.0014
K-PtSn@MFI-600H$_2$-0h[b]	3.2 ± 0.3	2.072 ± 0.006	0.0095 ± 0.0018	7.9 ± 0.3	0.0053
K-PtSn@MFI-600H$_2$-1h[b]	3.0 ± 0.1	2.067 ± 0.003	0.0050 ± 0.0006		0.0014
K-PtSn@MFI-600H$_2$-3h[b]	3.1 ± 0.2	2.065 ± 0.004	0.0055 ± 0.0010		0.0037
K-PtSn@MFI-600H$_2$-6h[b]	3.1 ± 0.1	2.068 ± 0.003	0.0055 ± 0.0007		0.0028
K-PtSn@MFI-600H$_2$-12h	3.2 ± 0.2	2.057 ± 0.005	0.0059 ± 0.0014		0.0046
K-PtSn@MFI-600H$_2$-22h[b]	3.3 ± 0.4	2.049 ± 0.006	0.0064 ± 0.0021		0.0138

[a]The fits were performed on the first coordination shell (ΔR = 2.0-3.0 Å) over FT of the $k^1k^2k^3$-weighted χ(k) functions performed in the Δk = 3.6-16.7 Å^{-1} interval. The standard Pt foil was fitted individually while the samples were fitted using a co-refinement approach resulting into one N_{Pt-Pt}, R and σ^2 for each sample and one ΔE_0 common for all samples. Non optimized parameters are recognizable by the absence of the corresponding error bar. $S_0^2 = 0.89$

[b]The fits were performed on the first coordination shell (ΔR = 1.0-2.0 Å) over FT of the $k^1k^2k^3$-weighted χ(k) functions performed in the Δk = 2.8-11.0 Å^{-1} interval. The standards SnO_2 and SnO were fitted individually while the four samples were fitted using a co-refinement approach resulting into one N_{Sn-O}, R_{Sn-O}, σ^2 per sample and one ΔE_0 for each series. Non optimized parameters are recognizable by the absence of the corresponding error bar. SnO_2 $S_0^2 = 0.89$; SnO $S_0^2 = 1.0$.

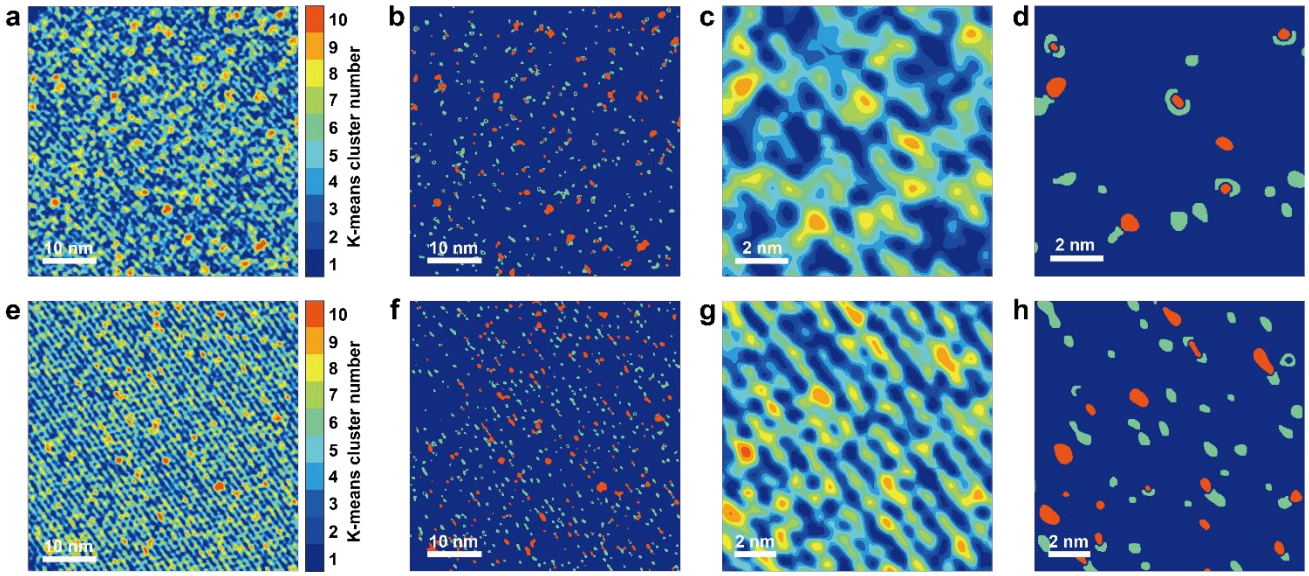

Figure 3. Distribution of Pt and Sn species. K-means clustering analysis on high-resolution scanning transmission electron microscopy images obtained under *quasi in situ* conditions (a-d) and *ex situ* conditions (e-h) with the K-PtSn@MFI-600H_2-6h sample. The results of K-means clustering analysis on the experimental HR HAADF-STEM images are shown in (a, c, e and g) and the corresponding maps of the distribution of Pt (red) and Sn (green) species are shown in (b, d, f and h). The K-means clustering analysis was performed on the basis of the different Z-contrast of Pt and Sn species in HAADF-STEM images.

Direct Measurement of PtSn clusters by *quasi in situ* TEM

To avoid the oxidation of PtSn clusters in air, TEM experiments were carried out using a vacuum transfer TEM holder when transferring the reduced sample into the microscope (see details in **Supplementary Figure 19**)[25,26]. As shown in **Supplementary Figures 20-23**, well distributed subnanometric Pt clusters are observed in the *quasi in situ* TEM experiments and their location is determined to be in the 10R sinusoidal channels according to the STEM-iDPC images (**Supplementary Figures 24-31**). Due to the very small size of the PtSn clusters and the relatively low stability of the zeolite support under the electron beam, it is extremely difficult to obtain the information on the distribution of Pt and Sn by conventional X-ray energy dispersive spectroscopy, though that technique can work quite well on bimetallic nanoparticles[27,28]. In order to quantitatively describe the spatial distribution of subnanometric Pt and Sn in the various K-PtSn@MFI samples, the HR HAADF-STEM images were analyzed by a modified K-means clustering method (an

unsupervised machine learning algorithm for signal processing as explained in **Supplementary Figures 32-S33**)[17]. As can be seen in **Figure 3**, only Pt and Sn species that can be identified by the K-means clustering analysis based on the different Z-contrast of Pt and Sn species in the HR HAADF-STEM image can be considered. We must note that the analysis only detects small Sn clusters adjacent to small Pt clusters, because of the lack of sensitivity to locate single Sn atoms, as discussed in our previous work[17]. As shown in **Figure 4** and **Supplementary Figure 34-37**, we have found that as the reduction time increases, the percentage of bimetallic PtSn clusters in the K-PtSn@MFI sample also increases, reaching >50% in both K-PtSn@MFI-600H_2-12h and K-PtSn@MFI-600H_2-22h. We note that this analysis is only semi-quantitative, taking into account that a) HAADF-STEM does not provide sufficient Z-contrast to detect isolated Sn atoms that may be contacting the Pt clusters, and b) part of the 3D information of the zeolite is lost in the 2D image processing. However, our K-means clustering analysis identifies a gradually greater contact between Pt and Sn when increasing the reduction time. Independent observations of the Pt performance in CO chemisorption and propane dehydrogenation experiments suggest that the number of Pt clusters that contain Sn is actually much greater than 50% at the longest reduction times (here-in-below). Considering the size of the metal clusters confined in the sinusoidal channels of MFI (**Figure 1**), the lack of Pt/Sn interactions detectable by EXAFS, and the clear presence of Sn-O and Pt-Pt bonds (**Table 1**), we speculate that a representative reduced bimetallic PtSn cluster in this sample is comprised of 8-10 atoms Pt core and a very few Sn atoms making direct contact with the support oxygens. Nevertheless, a significant fraction of the Sn seems to exist as partially reduced SnO_{2-x} clusters that do not directly interact with the Pt, rising strong Sn-O signals in the EXAFS spectra.

For comparison, we have also carried out the same K-means clustering analysis on the HR HAADF-STEM images for samples that were exposed to atmospheric air after the H_2 treatments, prior to introduction into the microscope (see **Figure 3e-h**). When the reduced samples were exposed to atmospheric air, the number of Sn in close proximity to Pt decays significantly (**Figure 4**). At very low reduction times (K-PtSn@MFI-600H_2-0h), the percentage of Pt clusters interacting with Sn is very low (~10 %), and increases to approximately ~20% as the reduction time is prolonged for the next 22 h (**Supplementary Figures 38-43)**. We infer that the two metals segregate as the oxophilic Sn is mobilized in contact with air, as widely observed with bimetallic nanoparticles in the literature[29-31].

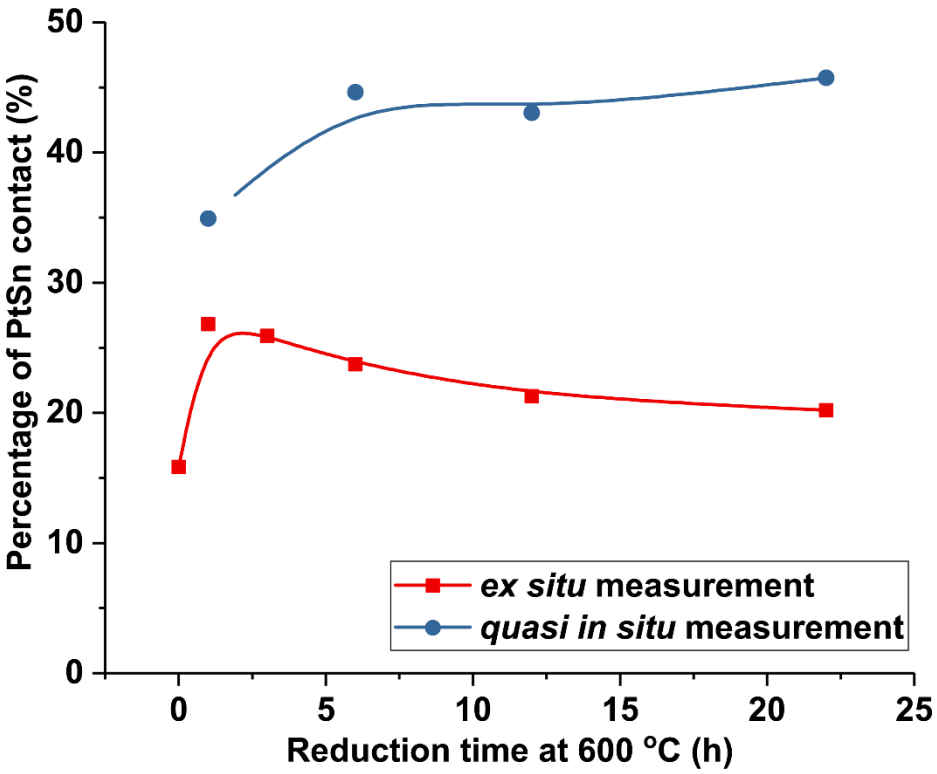

Figure 4. Percentage of PtSn contacts in various K-PtSn@MFI samples. The percentage of PtSn interactions between subnanometric Pt and Sn species obtained by K-means clustering analysis on high-resolution scanning transmission electron microscopy images for reduced samples that were exposed to atmospheric air prior to imaging (red) and samples that were not (blue)

As noted above, the K-means clustering analysis is based on two-dimensional projection images, while the K-PtSn@MFI zeolite is a three-dimensional material. Moreover, the complicated structure of K-PtSn@MFI also brings difficulty to distinguish the Pt and Sn species, which has already been explained in our previous work[17]. Despite the artifacts that may be introduced by the above factors, the percentages of contacted PtSn clusters in K-PtSn@MFI samples measured under *quasi in situ* conditions are clearly higher than the values obtained in the corresponding *ex situ* experiments, confirming the influence of the reduction treatment on the spatial relationship between Pt and Sn species, and stressing the necessity to protect the reduced sample from air in order to get reliable results.

Subnanometric Pt clusters seem to have a higher probability to interact with subnanometric Sn species after long-time reduction treatment. Such geometric characteristic indicate that Pt clusters probably are firstly reduced by H_2, consistent with previous work showing full Pt reduction at <200

ºC[14], and then followed by the reduction of Sn(IV) species and subsequent migration to meet the Pt clusters, also consistent with the time-resolved Pt L_{III}-edge and Sn K-edge XANES spectra of the pristine K-PtSn@MFI in H_2 reported here (**Supplementary Figures 44-45**).

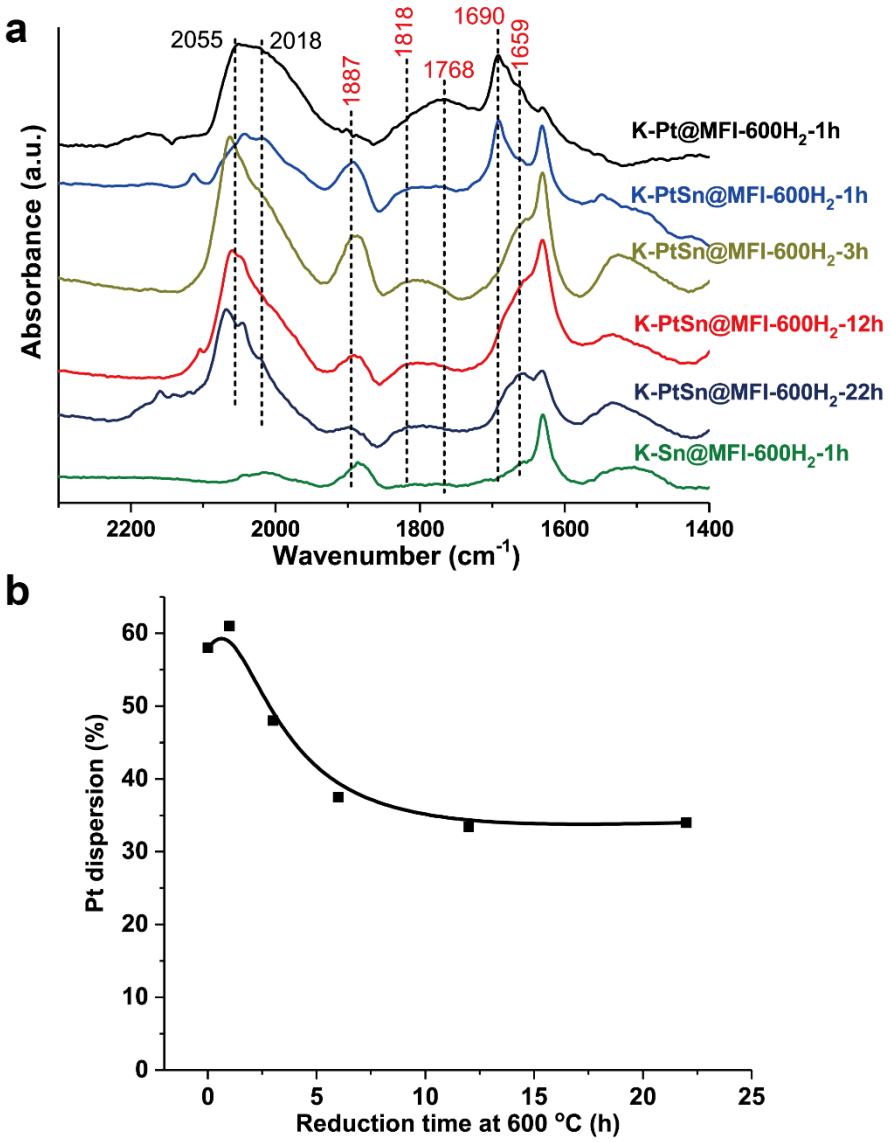

Figure 5. CO-IR spectra and CO-chemisorption results. (a) CO-IR spectra of K-Pt@MFI, K-Sn@MFI and K-PtSn@MFI samples after different pre-reduction treatment. The samples were reduced at 600 ºC by H_2 for a given time and then transfer to IR cell and reduced again in the IR cell at 450 ºC by H_2 for 2 h before the measurements. The CO-IR spectra were recorded at room temperature. The intensity in Y axis indicates actual absorbance, which was normalized according to the mass of solid sample used in the IR measurement. (b) The dispersion of Pt in K-PtSn@MFI samples after different times of pre-reduction treatment by H_2 at 600 ºC. The sample was reduced by H_2 at 600 ºC for a given time and then measured by CO chemisorption. According to our repetitive measurements, the error for CO chemisorption is within ±6 %.

Characterization of PtSn clusters by CO adsorption

In order to detect possible Pt-Sn interaction in the reduced K-PtSn@MFI samples, we have employed IR spectroscopy using CO as a probe molecule (CO-IR) to investigate the electronic properties of Pt species. As shown in **Figure 5a**, the bimetallic K-PtSn@MFI samples show a band at ~1887 cm^{-1} that the monometallic K-Pt@MFI does not. This band is slightly blue shifted relative to that observed in the K-Sn@MFI sample, which can be inferred to CO adsorbed onto Pt-SnO_x sites. Interestingly, the contribution of this band decreases when increasing the pre-reduction time, as a reduction of Sn(IV) species occurs. Sn-edge XANES and EXAFS show, in contrast, that Sn species exist as highly dispersed SnOx and the averaged chemical states of Sn species in the whole sample is close to Sn(II), regardless of the reduction time (**Figure 2** and **Table 1**). We believe that the reduced Sn species in contact with Pt clusters represent a fraction of the total Sn species in the whole material, which is too small to be captured by an average technique such as EXAFS[24].

The formation of interactions between Pt clusters and partially reduced Sn species during the H_2 treatment is also reflected on the changes of CO adsorption bands in the range of 1850 to 1650 cm^{-1}. For the CO bands in this range, they should be associated to CO adsorbed on metal clusters[32-34]. The position of the bands is related to the electronic structure of the metal clusters, which is controlled by the chemical compositions, size and geometric structure. Therefore, it is difficult to assign the adsorption band to a specific type of species. Nevertheless, we can still see some trends of changes in the spectra caused by the pre-treatment by H_2. The μ^3-adsorption band of CO on Pt clusters (1690 cm^{-1}) can be observed in both K-Pt@MFI and K-PtSn@MFI-600H_2-1h and this band decreases drastically after 3 h of reduction treatment. On the other hand, the band at 1659 cm^{-1} also increases when comparing the K-PtSn@MFI-600H_2-1h spectrum with the K-PtSn@MFI-600H_2-3h spectrum. These changes indicate the modulation of the electronic structures of the Pt clusters during the H_2 treatment and may be related to the interaction between Pt and Sn species.

Nevertheless, the formation of PtSn nanoparticles is also confirmed by the decrease of CO-IR bands at 2018 cm^{-1} in the K-PtSn@MFI samples when increasing the reduction time from 1 to 3 h. The contribution of this band, which corresponds to CO adsorbed on highly under-coordinated Pt sites of nanoparticles[35], decreases notably when the K-PtSn@MFI sample was reduced for ≥3 h at 600 ºC by H_2, as more Sn adds to the cluster and inhibits CO to adsorb on the adjacent Pt atoms[36-38].

However, we do not observe Pt-Sn bonding by EXAFS, indicating that the fraction of PtSn nanoparticles in the whole sample is low, consistent with the fact that the vast majority of Pt retains the original Pt-Pt coordination (**Table 1**).

The formation of Pt clusters interacting with partially reduced Sn species in the reduced K-PtSn@MFI samples can be also inferred from the CO-chemisorption results. As displayed in **Figure 5b**, the apparent Pt dispersion decreases with the reduction time, especially from 0 to 6 h. Since the size of Pt remains almost unchanged according to the characterization results based on STEM and EXAFS, the decrease of exposed Pt surface should be caused by the formation of Pt-Sn interaction, in a scenario where partially reduced Sn species interact with the external surface of Pt clusters. Again, we note that the amount of Sn atoms interacting with the Pt clusters must be low, which causes the absence of Pt-Sn contribution in EXAFS spectra and a Pt dispersion of ~30% in the K-PtSn@MFI-600H_2-22h sample[39,40].

According to all the spectroscopic results discussed above (Sn-edge XANES and EXAFS results, CO-IR), it can be concluded that pre-reduction treatment induces the reduction of Sn (IV) species in the pristine K-PtSn@MFI sample and the reduced Sn species can interact with subnanometric Pt clusters. The structural evolution of Pt and Sn species starting from the pristine K-PtSn@MFI-air sample is schematized in **Figure 6**, in which we postulate that the reduction of Pt single atoms to Pt clusters, the reduction of atomically dispersed Sn(IV) to reduced Sn species, and the formation of PtSn bimetallic clusters occur stepwise, with a final PtSn cluster structure consisting of a few Pt atoms (we infer less than 15 based on the microscopy results) and a very few Sn atoms (e.g. 2-3) coordinated to their external surface, probably through Pt-O-Sn bonding. We note that the geometric and electronic features of these PtSn bimetallic clusters are not common in most conventional PtSn bimetallic catalysts[41,42].

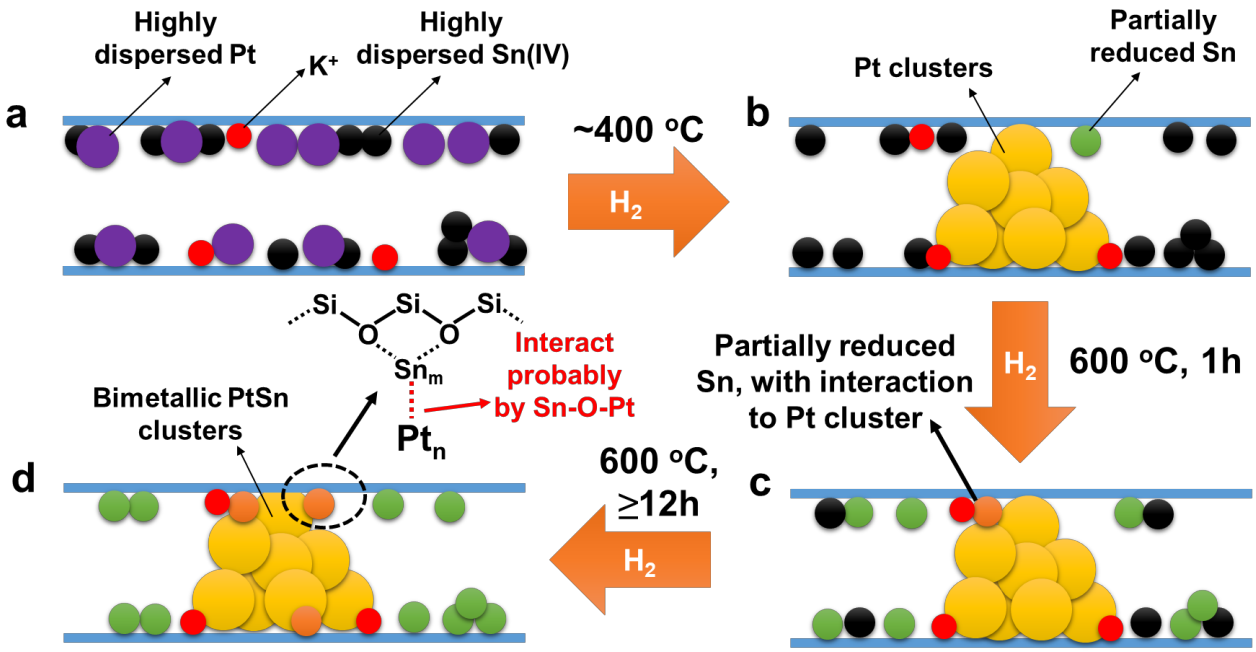

Figure 6. Structural evolution of K-PtSn@MFI during the reduction treatment with H_2. (a) In the pristine K-PtSn@MFI sample, both Pt and Sn exist as atomically dispersed species in the sinusoidal channels of MFI zeolite. (b) After reduction by H_2 at 400 °C, Pt single atoms will be reduced and form subnanometric Pt clusters while only a few of the Sn(IV) species will be reduced. (c) When the temperature is increased to 600 °C, most of the Sn(IV) species are reduced to Sn(II), but those reduced Sn species mainly remain separated from Pt clusters. (d) After being kept in H_2 flow for long time (⩾12 h), part of the reduced Sn species migrate to Pt clusters and bimetallic PtSn clusters with reduced Sn species interacting with the external surface of Pt clusters are formed in the sinusoidal 10R channels of MFI zeolite. It should be noted that, due to the complexity of the structures of PtSn clusters, the models proposed in this figure could be over simplified. PtSn clusters with different structures could exist in the working catalyst, as indicated by the CO-IR spectra.

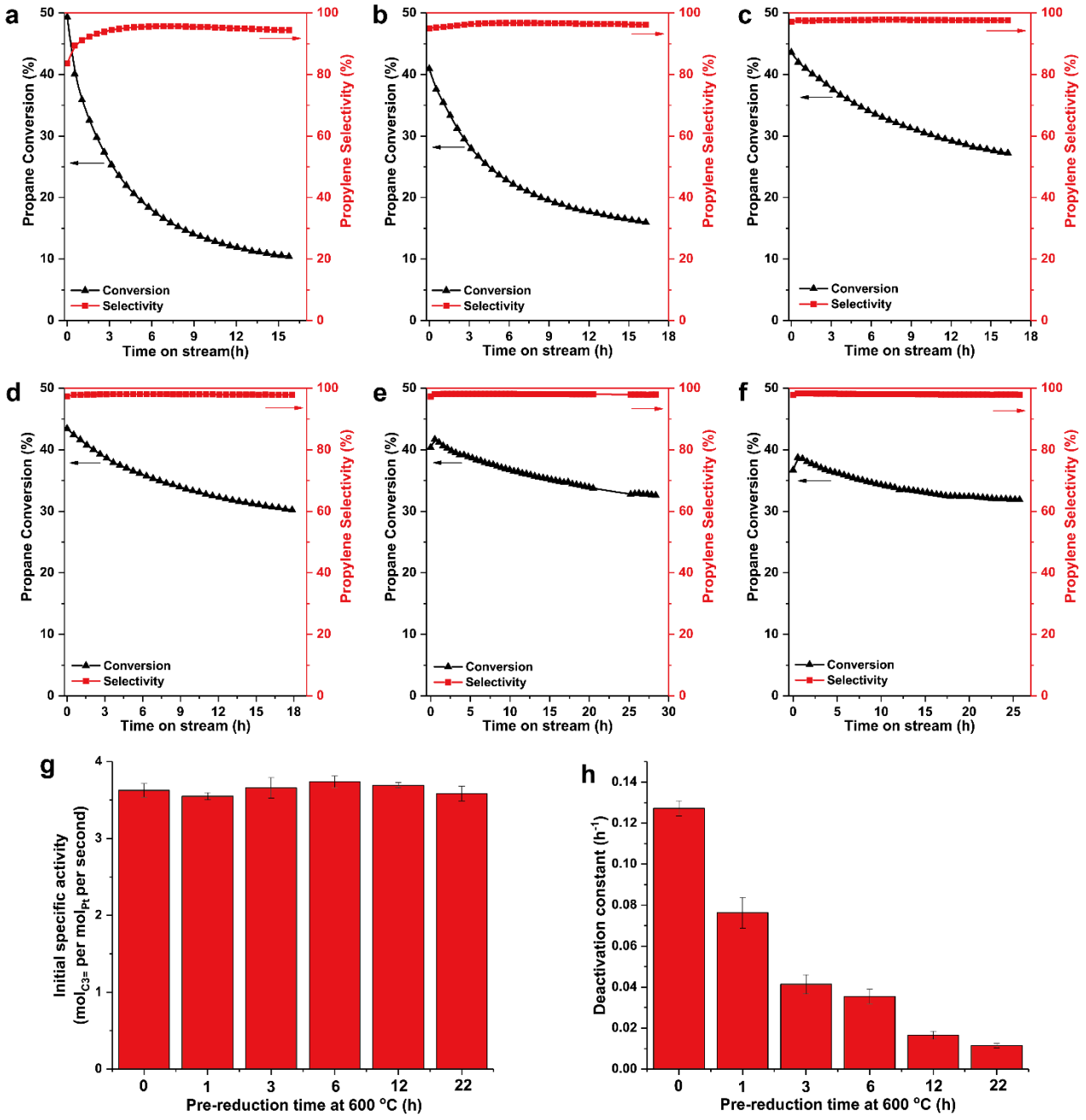

Figure 7. Catalytic performance for propane dehydrogenation reaction. Reaction conditions: 5 mL/min of propane, 16.5 mL/min of N_2, 600 °C, 20 mg of K-PtSn@MFI-600H_2 catalyst. The catalyst was reduced by H_2 flow of 35 mL/min at 600 °C for different times before the dehydrogenation reaction tests. (a) The K-PtSn@MFI-600H_2-0h catalyst was reduced by H_2 from room temperature up to 600 °C with a ramp rate of 10 °C/min. Once the temperature reached 600 °C, the atmosphere was switched to propane dehydrogenation feed gases. (b) K-PtSn@MFI-600H_2-1h, (c) K-PtSn@MFI-600H_2-3h, (d) K-PtSn@MFI-600H_2-6h, (e) K-PtSn@MFI-600H_2-12h, (f) K-PtSn@MFI-600H_2-22h. For the samples shown in (b-f), the catalyst was reduced reduced by H_2

from room temperature up to 600 ºC with a ramp rate of 10 ºC/min, and then kept at 600 ºC for a given time. All the initial activity values are below that corresponding to the thermodynamic equilibrium for propylene yield, which is close to 70% (assuming 100% selectivity to propylene). The analysis was carried out with an on-line GC with automated sample injector, allowing to achieve an error within ±3 % for each data point. (g) Initial specific activity for the production of propylene with K-PtSn@MFI catalyst after different pre-reduction treatment at 600 ºC. The specific activity was calculated using the initial activity shown in (a-f). (h) Deactivation constant of various K-PtSn@MFI catalysts during the propane dehydrogenation reaction at 600 ºC. These values were calculated based on the data presented in (a-f) according to the following formula: $\ln[(1-X_{final})/X_{final}] = k_d*T + \ln[(1-X_{intial})/X_{intial}]$. X_{final} and $X_{initial}$ are the propane conversion at the final and initial stage, respectively. T, the lifetime of the catalyst measured in the catalytic test. k_d, deactivation constant. The error bars were determined by three independent catalytic tests under given conditions. The error for initial specific activity and deactivation constant in all the samples is within ±6 % and ±12 %, respectively.

Catalytic performance for propane dehydrogenation

To show the implication of the structural changes during H_2 reduction treatment, we have tested various K-PtSn@MFI samples for propane dehydrogenation. Along this study, we have used a short contact time to get conversions below the thermodynamic equilibrium (~70%), to better study the influence of pre-reduction treatment. The catalytic performance of K-PtSn@MFI after different pre-reduction treatments is shown in **Figure 7**. As can be seen in **Figure 7a**, after a short-time pre-reduction treatment (the K-PtSn@MFI-600H_2-0h sample), the initial conversion is ~50% (the thermodynamic conversion for propane to propylene and H_2 is ~70% at a theoretical 100 % propylene selectivity), and the selectivity to propylene is ~82%, giving ~18% hydrogenolysis products (methane, ethane and ethylene) and a very small amount of aromatics. A fast decay of the activity was observed after ~15 h of time on stream, caused by the blockage of the Pt sites by coke. When the starting K-PtSn@MFI sample was kept in H_2 at 600 ºC for 1 h before the PDH reaction (activation condition used in our previous work[17], see **Figure 7b**), then the initial activity for propane dehydrogenation decreased slightly while the selectivity to propylene increased to 93%. More

importantly, the deactivation rate was also lower than the K-PtSn@MFI-600H_2-0h sample. If the pre-reduction time at 600 ºC was further increased to 3 h, 6 h and 12 h (**Figure 7c-7e**), the initial conversion of propane almost remained almost unchanged while the deactivation of the K-PtSn@MFI catalyst was significantly suppressed. The coke preferentially forms on the unselective Pt sites, therefore, the K-PtSn@MFI sample with higher initial selectivity also exhibits slower deactivation[43]. The slower deactivation is associated to the reductive atmosphere since thermal treatment in N_2 at 600 ºC cannot alleviate the deactivation (**Supplementary Figure 46**). However, if the K-PtSn@MFI sample was pre-reduced with H_2 for a longer time of 22 h (see **Figure 7f**), a slight decrease of the initial activity was observed, but high initial selectivity and very slow deactivation were achieved. Notice that in all the above catalytic tests, no H_2 was introduced in the feed gas. Slower deactivation and longer lifetime could be expected if H_2 was introduced, although with a penalty in the equilibrium conversion[44,45].

As can be seen in **Figure 7g-h**, the initial activity on a per Pt basis is almost the same regardless of the pre-reduction treatments from 0 to 22 h, while the deactivation constant varies drastically. This result is remarkable, since the number of Pt sites and their reactivity must remain high while Sn is incorporated to (selectively) modulate the Pt reactivity to avoid hydrogenolysis and coke formation reactions. In this sense, microscopy and EXAFS confirm not only that the K-PtSn@MFI samples remain ultra-dispersed after the various thermal treatments, but that the incorporation of Sn at the longest reduction times is just enough to greatly inhibit the deactivation by coke without compromising the dehydrogenation catalytic activity.

To further confirm the role of Sn, we have studied the influence of Sn loading in the K-PtSn@MFI sample on its catalytic performance (see **Supplementary Figures 47-51** and **Supplementary Discussion**). The sample with lower Sn loading gives lower initial selectivity to propylene and faster deactivation, which can be associated to lower amount of PtSn contacts in that sample. While in the case of the sample with high Sn loading, PtSn alloy nanoparticles (>2 nm) are formed due to the presence of plenty of defects in the MFI zeolite crystallites and the sintering of Pt species results in a decrease of activity. These results confirm the critical role of Sn on improving the selectivity to propylene and suppressing the catalyst deactivation. Furthermore, the results clearly show that the formation of bimetallic PtSn clusters is much more favorable when Pt and Sn are confined in the sinusoidal 10MR channels of MFI zeolite.

The used K-PtSn@MFI sample after propane dehydrogenation reaction tests has also been characterized by STEM. As shown in **Supplementary Figures 52-57**, no sintering of Pt clusters into larger particles has been observed in each of the samples after propane dehydrogenation reaction and the location of PtSn clusters in the 10R sinusoidal channels is also preserved, further confirming their high stability (**Supplementary Figures 58-61**). As shown in **Supplementary Figures 62-63**, the high initial activity and very slow deactivation as well as the size of subnanometric PtSn clusters has been preserved for three reaction cycles.

The good performance of the Pt species confined in the 10R channels of MFI is also reflected in the initial reactivity for propane dehydrogenation in comparison with literature results. We have summarized the catalyst activation conditions and catalytic performances of supported Pt catalysts in the recent literature (see **Supplementary Table 1**) and the initial activity of the K-PtSn@MFI-600H_2-22h sample on a per Pt basis is among the highest, at the same time that the deactivation rate is among the lowest. Compared to our previous work (catalyst activated by 1 h reduction at 600 ºC in H_2)[17], the optimized activation conditions developed in the current work lead to a 7-fold decrease in deactivation constant.

On the basis of the above results, it can be deduced that a long-time reduction treatment at 600 ºC is necessary to form subnanometric Pt clusters modified with partially reduced SnOx atoms or clusters, which show high activity, selectivity and stability for propane dehydrogenation. In additional experiments, we have observed that a shorter pre-reduction treatment at higher temperature (700 °C) on K-PtSn@MFI-air sample (K-PtSn@MFI-700H_2-1h) also results in subnanometric PtSn clusters in the sinusoidal channels (**Supplementary Figure 64**), showing similar high selectivity and very low deactivation rate in the propane dehydrogenation reaction (**Supplementary Figure 65**).

The amount of coke in the used K-PtSn@MFI samples after propane dehydrogenation reaction has been analyzed by TG-DSC. As shown in **Supplementary Figures 66-71**, the amount of coke in all the samples remain below 1 wt% but no correlation between stability and the amount of deposited coke has been found according to the TG-DSC results. The coke properties in the used catalysts have been studied by Raman spectroscopy. As shown in **Supplementary Figure 72**, the ratio of ***D*** band and ***G*** band in all the samples ranges from 0.45 to 0.5, exhibiting minor differences (see **Supplementary Table 2**). Therefore, it can be concluded that the amount of coke and the

physiochemical properties of the coke seem to be similar among the K-PtSn@MFI-600H_2 samples after different time of pre-reduction. From a structural point of view, the PtSn clusters are mainly located in the sinusoidal channels. Even though the coke formation is associated with catalytic events occurring at the metal surface, the resultant carbonaceous species seem not to remain directly blocking the active sites. The extended lifetime of the long-time reduced K-PtSn@MFI-600H_2-12h and K-PtSn@MFI-600H_2-22h sample could be associated to much less deposition of coke on PtSn clusters, leading to the low deactivation rate[46]. Since the deposition of coke on Pt-based catalyst for propane dehydrogenation reaction is related to the chemical composition of the bimetallic PtM particles[47], the results presented indicate that a minimal interaction between the two metals is sufficient is sufficient to suppress most of the coke, provided that the active species remain small (in the subnanometric regime) during the whole catalyst lifetime.

Finally, to show the potential of the K-PtSn@MFI catalyst activated under optimized conditions, we have tested the catalytic performance of K-PtSn@MFI under a more industrially relevant conditions (e.g. no N_2 dilution) for the propane dehydrogenation reaction. As presented in **Supplementary Figure 73**, the K-PtSn@MFI catalyst shows an initial propane conversion of ~20% at 550 ºC and a high initial selectivity to propylene (>97%) under a high weight-hour space velocity of ~118 h^{-1}. After nearly 70 h of time on stream, the propane conversion decreases very slowly from ~20% to ~17%, demonstrating the outstanding performance of the K-PtSn@MFI catalyst in this reaction.

Conclusions

The geometric and electronic structures of subnanometric bimetallic clusters in confined space can be different to the counterpart nanoparticles supported on open-structure carriers, which can lead to unique reactivity. Combining multiple *in situ* characterization techniques (both averaged techniques like XAFS and site-specific techniques like IR and TEM) is critical to elucidate the nature of the active sites in supported catalysts containing isolated atoms and/or clusters[48].

Methods

One-pot Synthesis of K-PtSn@MFI sample

Firstly, a tetrapropylammonium hydroxide (TPAOH) solution was prepared by mixing 5.0 g K-free TPAOH solution (40 wt%, from Alfa-Aesar without K, product code: 17456.22) and 6.24 g TPAOH (20 wt% from Sigma-Aldrich, containing ~0.6 wt% of K, product code: 254533-100G) and 17.0 g of distilled water at room temperature. Then, 8.24 g Tetraethyl orthosilicate (TEOS) were hydrolyzed with tetrapropylammonium hydroxide solution (TPAOH) at room temperature for 6 h under stirring (500 rpm). The resultant solution was divided into two parts with the same weight. To each portion of the solution, 80 μL of H_2PtCl_6 aqueous (0.38 mol/L), 50 mg of $SnCl_4{\cdot}5H_2O$ and 150 μL of ethylenediamine were added to the above solution and the mixture kept under stirring for 20 min. The resultant yellow solution was then transferred to Teflon-lined autoclaves and heated in an electric oven at 175 ºC for 96 h under static conditions. The amounts of Pt, Sn and K in the final product were ~0.4 wt%, ~0.9 wt% and ~0.6 wt%, respectively. After the hydrothermal process, the solid product was isolated by filtration and washed with distilled water and acetone and then dried at 60 ºC. Then the solid sample was calcined under air flow at 560 ºC for 8 h and then at 600 ºC for 2 h.

Characterization

Powder X-ray diffraction (XRD) was performed with a HTPhilips X'Pert MPD diffractometer equipped with a PW3050 goniometer using Cu Kα radiation and a multisampling handler.

Samples for electron microscopy studies were prepared by dropping the suspension of the solid samples in CH_2Cl_2 directly onto holey-carbon coated copper grids. Electron Microscopy measurements were performed using two types of microscopes. Thus, non-corrected JEOL 2100F microscope operating at 200 kV both in transmission (TEM) and scanning-transmission modes (STEM) was used to record High Angle Annular Dark Field (HAADF), Z-contrast, images at low resolution. High-resolution HAADF-STEM and STEM-iDPC imaging was performed on a double aberration corrected (AC), monochromated, FEI Titan^3 Themis 60-300 microscope working at 300 kV. The last technique, iDPC (integrated-Differential Phase Contrast) imaging, provides in this microscope atomically resolved images in which the contrasts are related to the atomic number of the elements under the beam, instead of the roughly Z^2-dependent contrasts obtained in HAADF-STEM

images. By using a 4-segment detector, this technique allows imaging light elements, as it is the case of O, in the presence of heavier ones (Si, Z=14) under very low electron dose conditions, which is a key aspect in the atomic scale structural analysis of zeolites, which are very sensitive to electron beams. In particular, 2048×2048 HAADF-iDPC image pairs were recorded simultaneously using a convergence angle of 18.6 mrad and a camera length of 91 mm. This configuration allowed us to optimize the collection of the signals on the HAADF and FEI DF4 detectors. In order to limit the damage by the electron beam, a fast image recording protocol was used by combining a beam current of 10-30 pA, a 1.25-2.5 µs dwell time and an automated fine-tuning alignment of A1 and C1 using the OptiSTEM software. To obtain images with good quality, the beam current and image acquisition time should be optimized according to the stability of the sample under the beam.

For the *quasi in situ* TEM studies on the K-PtSn@MFI samples, the powder of the pristine K-PtSn@MFI-air sample was reduced by H_2 flow at 600 ºC for a given time (from 1 h to 22 h) and then the reactor for reduction treatment was closed and transfer to glove box. The preparation of the grid for TEM measurement was carried out in the glove box to protect the sample from oxidation by air. After the sample preparation, the TEM grid is sealed in the vacuum transfer TEM holder and then transfer to the electron microscope for HRSTEM-iDPC measurements.

To determine the spatial distribution of the metallic species within the zeolite framework, a specific methodology for the digital analysis of the experimental images has been developed and coded in a home-made Matlab script. First, to improve the signal-to-noise, the HR HAADF STEM images were denoised by combining the Anscomb transform and Undecimated Wavelet Transforms (UWVT)[49]. Then, a user-independent, fully automated, segmentation of image contrasts by clustering techniques (K-means method) was applied to recognize and classify the metallic entities, which is a requirement to guarantee statistically meaningful and unbiased results.

To support the K-means clustering analysis and interpreting the details of the experimental images HR HAADF-STEM image simulation was carried out using TEMSIM software[50]. The complex structural models used as input in these simulations were built using the Rhodius software developed at UCA[51]. To approach as close as possible to the experimental imaging conditions, a mixture of Poisson and white Gaussian noise was added to the simulated images. Then, the same methodology used to analyze the experimental images was applied to the on-purpose noise-corrupted simulated images.

X-ray absorption experiments at the Pt (11564 eV) L_{III} and Sn (29200 eV) K-edges, were performed in ALBA synchrotron[52]. The beam was monochromatized using a Si (111) and (311) double crystals, respectively; harmonic rejection has been performed using Rh-coated silicon mirrors. The spectra were collected in transmission (Pt L_{III}-edge) and fluorescence (Sn K-edge) modes by means of the ionization chambers filled with appropriate gases (Pt L_{III}-edge: 95 % N_2 + 5 % Kr for I_0 and 17.1 % N_2 + 82.9 % Kr for I_1; Sn K-edge: 89.4 % N_2 + 10.6 % Kr for I_0 and 100 % Kr for I_1) and a fluorescence solid-state detector. Samples in the form of self-supported pellets of optimized thickness have been located inside an in-house built multipurpose cell described by Guilera allowing *in situ* experiments[53]. Several scans were acquired at each measurement step to ensure spectral reproducibility and good signal-to-noise ratio. The data reduction and extraction of the $\chi(k)$ function has been performed using Athena code. EXAFS data analysis has been performed using the Arthemis software[54]. Phase and amplitudes have been calculated by FEFF6 code. The values of E_0 (inflection point in the first derivative of XANES spectra) used for data alignment taken from literature were the following: 29200 eV for Sn metal, 29201 eV for SnO, 29204 eV for SnO_2 and 11564 eV for Pt metal.

IR spectra of adsorbed CO on Pt-zeolite and Sn-zeolite samples were recorded at room temperature with a Nexus 8700 FTIR spectrometer using a DTGS detector and acquiring at 4 cm^{-1} resolution. The K-PtSn@MFI samples were reduced at 600 ºC in an oven for different times and then transferred to an IR cell allowing in situ treatments in controlled atmospheres and temperatures from 25 °C to 500 °C has been connected to a vacuum system with gas dosing facility. For IR studies the samples were pressed into self-supported wafers and pre-treated in H_2 flow at 450 °C for 2 h followed by vacuum treatment (10^{-5} mbar). After activation the samples were cooled down to 25 °C under dynamic vacuum conditions followed by CO dosing at increasing pressure (0.4-8.5 mbar). IR spectra were recorded after each dosage of CO.

The dispersion of Pt in K-PtSn@MFI sample was estimated from CO adsorption using the double isotherm method on a Quantachrome Autosorb-1C equipment[55,56]. Prior to adsorption, the samples (200-300 mg) were reduced in situ in flowing pure H_2 (25 mL/min) at 600 ºC for a given time. After the reduction treatment, the samples were degassed at 1.33 Pa for 2 h at 600 ºC and then cool to ~40 ºC. Then pure CO was admitted and the first adsorption isotherm (i.e. the total CO uptake) was measured. After evacuation at 25 ºC, the second isotherm (i.e. the reversible CO uptake) was measured. The amount of chemisorbed CO was then obtained by subtracting the two isotherms. The

pressure range studied was 0.5-11 $\times 10^4$ Pa. The dispersion of Pt (D) was calculated from the amount of irreversibly adsorbed CO assuming a stoichiometry of Pt/CO=1. The mean particle size (d) of Pt was determined from chemisorption data assuming spherical geometry for the metal particle according to the procedure. Equations (1-3) are used to calculate the dispersion of Pt.

$D\ (\%)=N_m \times F_s \times M \times 10^4 / L$ (1)

N_m: chemisorption uptake expressed in mol of CO per gram of sample;

F_s: adsorption stoichiometry, which is 1 in our measurement;

M: molecular weight of the supported metal (Pt)

L: loading of the supported metal.

$d=6 \times L/(S_a \times Z \times 100)$ (2)

d: mean particle size

Z: density of the supported metal (Pt)

S_a: active surface area (m^2/g_{metal}) calculated from the following equation: $S_a=N_m \times F_s \times A_m \times N_a$ (3)

A_m: cross-sectional area occupied by each active surface Pt atom

N_a: Avogadro's constant

Trimethylphosphine oxide (TMPO, supplied by Alfa Aesar) was adsorbed to the different catalysts via dichloromethane solutions as probe molecules to study the coordination environment of Sn species by NMR. First, all catalysts were degassed for 4 h under dynamic vacuum at 573 K to remove any water adsorbed molecules. They were then transferred to a glove box to prevent any exposure to moisture, which could interact with metal sites in the catalysts or with TMPO molecules. A solution of 0.02 wt% TMPO was prepared with anhydrous dichloromethane in a glove box. 0.3 g of this solution was added to each catalyst (75 mg) in a vial, and the samples were left to stir overnight. Dichloromethane was fully removed by heating to 353 K for the duration of 6 h. Samples dosed with TMPO were packed under inert atmosphere into zirconia MAS NMR rotors with gastight caps for analysis. Metal and P contents were measured by ICP analysis to determine the TMPO:M ratio.

Catalytic studies of K-PtSn@MFI sample for propane dehydrogenation reactions.

The reaction was performed with a fix-bed reactor under atmospheric pressure using N_2/propane as

feed gas at 600 ºC. The products were analyzed by a GC which can detect cracking products (methane, ethene and ethane), propylene, C4, C5 and aromatics. Before reaction, the K-PtSn@MFI catalyst was reduced by H_2 flow (35 mL/min) at 600 ºC for a given time with a ramp rate of 10 ºC/min from room temperature up to 600 ºC. After the reduction pre-treatment, the atmosphere was changed to reaction feed gas (5 mL/min of propane and 16 mL/min of N_2 as balanced gas). The analysis was carried out with an on-line GC with automated sample injector, allowing to achieve an error within ±3 % for each data point.

Data availability

All the data needed to support the plots and evaluate the conclusions within this article are present within it and the Supplementary Information, or are available from the corresponding author upon reasonable request.

Code availability

The codes used in this work for image analysis are available from the corresponding author upon reasonable request.

References

1. Liu, L. & Corma, A. Metal Catalysts for Heterogeneous Catalysis: From Single Atoms to Nanoclusters and Nanoparticles. *Chem. Rev.* **118**, 4981-5079 (2018).
2. An, K. & Somorjai, G. A. Nanocatalysis I: Synthesis of Metal and Bimetallic Nanoparticles and Porous Oxides and Their Catalytic Reaction Studies. *Catal. Lett.* **145**, 233-248 (2014).
3. Ferrando, R., Jellinek, J. & Johnston, R. L. Nanoalloys: from theory to applications of alloy clusters and nanoparticles. *Chem. Rev.* **108**, 845-910 (2008).
4. Yu, W., Porosoff, M. D. & Chen, J. G. Review of Pt-based bimetallic catalysis: from model surfaces to supported catalysts. *Chem. Rev.* **112**, 5780-5817 (2012).
5. Resasco, D. E. Dehydrogenation–Heterogeneous. Encyclopedia of Catalysis, I. Horváth eds. (2002).
6. Vora, B. V. Development of Dehydrogenation Catalysts and Processes. *Top. Catal.* **55**, 1297-1308 (2012).
7. Sattler, J. J., Ruiz-Martinez, J., Santillan-Jimenez, E. & Weckhuysen, B. M. Catalytic dehydrogenation of light alkanes on metals and metal oxides. *Chem. Rev.* **114**, 10613-10653 (2014).
8. Sanfilippo, D. & Miracca, I. Dehydrogenation of paraffins: synergies between catalyst design and reactor engineering. *Catal. Today* **111**, 133-139 (2006).
9. Redekop, E. A. *et al.* Delivering a Modifying Element to Metal Nanoparticles via Support: Pt–Ga Alloying during the Reduction of Pt/Mg(Al,Ga)Ox Catalysts and Its Effects on Propane Dehydrogenation. *ACS. Catal.* **4**, 1812-1824 (2014).
10. Deng, L. *et al.* Dehydrogenation of Propane over Silica-Supported Platinum-Tin Catalysts Prepared by Direct Reduction: Effects of Tin/Platinum Ratio and Reduction Temperature. *ChemCatChem* **6**, 2680-2691 (2014).
11. Filez, M.; Redekop, E. A.; Poelman, H.; Galvita, V. V.; Marin, G. B. Advanced elemental characterization during Pt-In catalyst formation by wavelet transformed X-ray absorption spectroscopy. *Anal. Chem.* **87**, 3520-3526 (2015).
12. Searles, K. *et al.* Highly Productive Propane Dehydrogenation Catalyst Using Silica-Supported Ga-Pt Nanoparticles Generated from Single-Sites. *J. Am. Chem. Soc.* **140,** 11674-11679 (2018).
13. Liu, L. *et al.* Generation of subnanometric platinum with high stability during transformation of a 2D zeolite into 3D. *Nat. Mater.* **16**, 132-138 (2017).
14. Moliner, M. *et al.* Reversible Transformation of Pt Nanoparticles into Single Atoms inside High-Silica Chabazite Zeolite. *J. Am. Chem. Soc.* **138**, 15743-15750 (2016).
15. Liu, L. *et al.* Evolution and stabilization of subnanometric metal species in confined space by in situ TEM. *Nat. Commun.* **9**, 574 (2018).
16. Liu, Y. *et al.* A General Strategy for Fabricating Isolated Single Metal Atomic Site Catalysts in Y Zeolite. *J. Am. Chem. Soc.* **141**, 9305-9311 (2019).
17. Liu, L. *et al.* Regioselective generation and reactivity control of subnanometric platinum clusters in zeolites for high-temperature catalysis. *Nat. Mater.* **18**, 866-873 (2019).
18. Lazic, I., Bosch, E. G. T. & Lazar, S. Phase contrast STEM for thin samples: Integrated differential phase contrast. *Ultramicroscopy* **160**, 265-280 (2016).
19. Yucelen, E., Lazic, I. & Bosch, E. G. T. Phase contrast scanning transmission electron microscopy imaging of light and heavy atoms at the limit of contrast and resolution. *Sci. Rep.* **8**,

2676 (2018).
20. Lewis, J. D. *et al.* Distinguishing Active Site Identity in Sn-Beta Zeolites Using ^{31}P MAS NMR of Adsorbed Trimethylphosphine Oxide. *ACS Catal.* **8**, 3076-3086 (2018).
21. Uemura, Y. *et al.* In situ time-resolved XAFS study on the structural transformation and phase separation of Pt3Sn and PtSn alloy nanoparticles on carbon in the oxidation process. *Phys. Chem. Chem Phys.* **13**, 15833-15844 (2011).
22. Ramallo-López, J. M. *et al.* XPS and XAFS Pt $L_{2,3}$-Edge Studies of Dispersed Metallic Pt and PtSn Clusters on SiO_2 Obtained by Organometallic Synthesis: Structural and Electronic Characteristics. *J. Phys. Chem. B* **107**, 11441-11451 (2003).
23. Deng, L. *et al.* Elucidating strong metal-support interactions in Pt–Sn/SiO_2 catalyst and its consequences for dehydrogenation of lower alkanes. *J. Catal.* **365**, 277-291 (2018).
24. Zhang, B. *et al.* Exceptional electrochemical performance of freestanding electrospun carbon nanofiber anodes containing ultrafine SnOx particles. *Energy Environ. Sci.* **5**, 9895 (2012).
25. Collins, S. E. *et al.* The role of Pd–Ga bimetallic particles in the bifunctional mechanism of selective methanol synthesis via CO_2 hydrogenation on a Pd/Ga_2O_3 catalyst. *J. Catal.* **292**, 90-98 (2012).
26. Ogata, K. *et al.* Evolving affinity between Coulombic reversibility and hysteretic phase transformations in nano-structured silicon-based lithium-ion batteries. *Nat. Commun.* **9**, 479 (2018).
27. Cui, C., Gan, L., Heggen, M., Rudi, S. & Strasser, P. Compositional segregation in shaped Pt alloy nanoparticles and their structural behaviour during electrocatalysis. *Nat. Mater.* **12**, 765-771 (2013).
28. Pei, Y. *et al.* Catalytic properties of intermetallic platinum-tin nanoparticles with non-stoichiometric compositions. *J. Catal.* **374**, 136-142 (2019).
29. Freakley, S. J. *et al.* Palladium-tin catalysts for the direct synthesis of H_2O_2 with high selectivity. *Science* **351**, 965-968 (2016).
30. Mayrhofer, K. J.; Juhart, V.; Hartl, K.; Hanzlik, M.; Arenz, M. Adsorbate-Induced Surface Segregation for Core-Shell Nanocatalysts. *Angew. Chem. Int. Ed.* **48**, 3529-3531 (2009).
31. Peng, L., Ringe, E., Van Duyne, R. P. & Marks, L. D. Segregation in bimetallic nanoparticles. *Phys. Chem. Chem Phys.* **17**, 27940-27951 (2015).
32. Li, G.-J., Fujimoto, T., Fukuoka, A. & Ichikawa, M. Ship-in-Bottle synthesis of Pt_9-Pt_{15} carbonyl clusters inside NaY and NaX zeolites, in-situ FTIR and EXAFS characterization and the catalytic behaviors in ^{13}CO exchange reaction and NO reduction by CO. *Catal. Lett.* **12**, 171-185 (1992).
33. Gruene, P., Fielicke, A., Meijer, G. & Rayner, D. M. The adsorption of CO on group 10 (Ni, Pd, Pt) transition-metal clusters. *Phys. Chem. Chem Phys.* **10**, 6144-6149 (2008).
34. Serykh, A. I. *et al.* Stable subnanometre Pt clusters in zeolite NaX via stoichiometric carbonyl complexes: Probing of negative charge by DRIFT spectroscopy of adsorbed CO and H_2. *Phys. Chem. Chem Phys.* **2**, 5647-5652 (2000).
35. Garnier, A., Sall, S., Garin, F., Chetcuti, M. J. & Petit, C. Site effects in the adsorption of carbon monoxide on real 1.8nm Pt nanoparticles: An Infrared investigation in time and temperature. *J. Mol. Catal. A: Chem.* **373**, 127-134 (2013).
36. Corma, A., Serna, P., Concepcion, P. & Calvino, J. J. Transforming nonselective into chemoselective metal catalysts for the hydrogenation of substituted nitroaromatics. *J. Am. Chem. Soc.* **130**, 8748-8753 (2008).

37. Concepcion, P. *et al.* The promotional effect of Sn-beta zeolites on platinum for the selective hydrogenation of alpha,beta-unsaturated aldehydes. *Phys. Chem. Chem Phys.* **15**, 12048-12055 (2013).
38. de Menorval, L.-C., Chaqroune, A., Coq, B. & François Figueras, a. Characterization of mono- and bi-metallic platinum catalysts using CO FTIR spectroscopy Size effects and topological segregation. *J. Chem. Soc., Faraday Trans.* **93**, 3715-3720 (1997).
39. Balakrishnan, K. A chemisorption and XPS study of bimetallic Pt-Sn/Al_2O_3 catalysts. *J. Catal.* **127**, 287-306 (1991).
40. Panja, C. & Koel, B. E. Probing the Influence of Alloyed Sn on Pt(100) Surface Chemistry by CO Chemisorption. *Israel J. Chem.* **38**, 365-374 (1998).
41. Liu, Z., Jackson, G. S. & Eichhorn, B. W. PtSn intermetallic, core-shell, and alloy nanoparticles as CO-tolerant electrocatalysts for H_2 oxidation. *Angew. Chem. Int. Ed.* **49**, 3173-3176 (2010).
42. Wang, X. *et al.* Pt/Sn Intermetallic, Core/Shell and Alloy Nanoparticles: Colloidal Synthesis and Structural Control. *Chem. Mater.* **25**, 1400-1407 (2012).
43. Redekop, E. A. *et al.* Early stages in the formation and burning of graphene on a Pt/Mg(Al)Ox dehydrogenation catalyst: A temperature- and time-resolved study. *J. Catal.* **344**, 482-495 (2016).
44. Shi, L. *et al.* Al_2O_3 Nanosheets Rich in Pentacoordinate Al^{3+} Ions Stabilize Pt-Sn Clusters for Propane Dehydrogenation. *Angew. Chem. Int. Ed.* **54**, 13994-13998 (2015).
45. Sattler, J. J., Beale, A. M. & Weckhuysen, B. M. Operando Raman Spectroscopy Study on the Deactivation of Pt/Al_2O_3 and Pt-Sn/Al_2O_3 Propane Dehydrogenation Catalysts. *Phys. Chem. Chem. Phys.* **15**, 12095-12103 (2013).
46. Vu, B. K. *et al.* Location and structure of coke generated over Pt–Sn/Al_2O_3 in propane dehydrogenation. *J. Ind. Eng. Chem.* **17**, 71-76 (2011).
47. Vu, B. K. *et al.* Pt–Sn Alloy Phases and Coke Mobility over Pt–Sn/Al_2O_3 and Pt–Sn/$ZnAl_2O_4$ Catalysts for Propane Dehydrogenation. *Appl. Catal. A: Gen.* **400**, 25-33 (2011).
48. Liu, L. *et al.* Determination of the Evolution of Heterogeneous Single Metal Atoms and Nanoclusters under Reaction Conditions: Which Are the Working Catalytic Sites? *ACS Catal.* **9**, 10626-10639 (2019).
49. López-Haro, M. *et al.* A Macroscopically Relevant 3D-Metrology Approach for Nanocatalysis Research. *Part. Part. Syst. Charact.* **35**, 1700343 (2018).
50. Kirkland, E. J. *Advanced Computing in Electron Microscopy*. Springer, **2010**.
51. Bernal, S. *et al.* The interpretation of HREM images of supported metal catalysts using image simulation: profile view images. *Ultramicroscopy* **72**, 135-164 (1998).
52. Simonelli, L. *et al.* CLÆSS: The hard X-ray absorption beamline of the ALBA CELLS synchrotron. *Cogent Physics* **3**, 1231987 (2016).
53. Guilera, G., Rey, F., Hernández-Fenollosa, J. & Cortés-Vergaz, J. J. One body, many heads; the Cerberus of catalysis. A new multipurpose in-situ cell for XAS at ALBA. *J. Phys. Conference Series* **430**, 012057 (2013).
54. Ravel, B. & Newville, M. ATHENA, ARTEMIS, HEPHAESTUS: data analysis for X-ray absorption spectroscopy using IFEFFIT. *J. Synchrotron Rad.* **12**, 537-541 (2005).
55. Yin, F., Ji, S., Wu, P., Zhao, F. & Li, C. Deactivation behavior of Pd-based SBA-15 mesoporous silica catalysts for the catalytic combustion of methane. *J. Catal.* **257**, 108-116 (2008).
56. Allian, A. D. *et al.* Chemisorption of CO and mechanism of CO oxidation on supported platinum nanoclusters. *J. Am. Chem. Soc.* **133**, 4498-4517 (2011).

Author Contributions

A.C. conceived the project, directed the study and wrote the manuscript. L.L. carried out the synthesis, structural characterizations, catalytic measurements and collaborated in writing the manuscript. M.L.-H., R.M. and J.J.C. carried out the quasi in situ high-resolution STEM measurements and image analysis. C.W.L. carried out the analysis of XAS data. L.L. and L.S. contributed to the collection of XAS data in ALBA synchrotron. S.R.-B. carried out the ^{31}P NMR measurements. P.C. carried out the CO-IR adsorption experiments. A.S. and P.S. contributed to the experimental design and data interpretation. All the authors discussed the results and contributed to the formation of the manuscript.

Acknowledgements

This work has been supported by the European Union through the European Research Council (grant ERC-AdG-2014-671093, SynCatMatch) and the Spanish government through the "Severo Ochoa Program" (SEV-2016-0683). L.L. thanks ITQ for providing a contract. The authors also thank Microscopy Service of UPV for the TEM and STEM measurements. The XAS measurements were carried out in CLAESS beamline of ALBA synchrotron. We would like to thank Giovanni Agostini for his kind support on the analysis of XAS data. High-resolution STEM measurements were performed at DME-UCA in Cadiz University with financial support from FEDER/MINECO (MAT2017-87579-R and MAT2016-81118-P). C.W.L. thanks CAPES (Science without Frontiers - Process no. 13191/13-6) for a predoctoral fellowship. The financial support from ExxonMobil on this project is also greatly acknowledged.